The mechanical properties of the organs and tissues of humans can be displayed by virtual reality techniques [21,22]. In particular, stiffness and force interactions are demonstrated by using a haptic device, which gives the operator force feedback directly [23–25]. Ladjal et al. used a haptic device to display the cell indentation process and simulate AFM experiments [26,27]. They developed a computer-based training system to simulate real-time ES cell indentation procedures in virtual environments through the combination of a haptic device and finite element simulations [27]. Thus, haptic devices are very useful communication tools for sharing the mechanical properties and information of a cell.

In this study, we constructed a simple virtual reality system using a haptic device that displays the mechanical properties of cells as determined by AFM nanoindentation experiments. To homogeneously display various types of cell morphology in this system, we measured and presented the mechanical properties of cells at floating state, because the morphology of floating cell is almost spherical irrespective of cell type. This system virtually displays the dispersion of the Young's modulus of a cell and the differences in Young's modulus between cell types. Using this system, we can directly recognize the mechanical information of a cell and share its perceived properties with others.

Materials and Methods

Materials

A tipless probe (TL-CONT; spring constant: 0.03 N/m) was purchased from Nanosensors (Neuchatel, Switzerland). Cell culture medium was purchased from Nacalai Tesque (Kyoto, Japan), and fetal bovine serum (FBS) was purchased from JRH Biosciences (Lenexa, KS). Antibiotics were purchased from Sigma-Aldrich (St. Louis, MO). Human bone marrow-derived mesenchymal stem cells (hMSCs) were obtained from a donor (age, 39 years) with written informed consent as previously described [28]. The study was approved by the ethics committee of National Institute of Advanced Industrial Science and Technology. HEK293 cells were obtained from Health Science Research Resources Bank (Osaka, Japan). Biocompatible Anchor for Membrane (BAM; SUNBRIGHT OE-020CS) was purchased from NOF CORPORATION (Tokyo, Japan). Spherical silica beads (4 μm in diameter) were purchased from Ube-Nitto Kasei (Tokyo, Japan). A haptic device, Falcon, was purchased from Novint Technologies Inc (Albuquerque, NM). A PC, the performance of which is shown in Table 1, was purchased from Sony corporation (Tokyo, Japan). Other reagents were obtained from Sigma-Aldrich, Wako Pure Chemical Industries Ltd. (Osaka, Japan), or Life Technologies Japan Ltd. (Tokyo, Japan).

Preparation of BAM-coated dishes

The BAM-coated dishes (Fig. 1) were prepared as described previously with minor modifications [29]. Briefly, polystyrene tissue culture dishes were coated with 5% BSA in PBS for 1 h. After washing with PBS, the surfaces were treated with 1 mM BAM in PBS for 1 h. Then, the BAM-coated dishes were washed and dried.

Table 1. System performance.

CPU	Intel core i3 (2.53 GHz)
Main memory	4.0 GB
OS	Microsoft Windows 7
Development environment	Microsoft Visual Studio 2010
Haptic device	Novint Falcon

doi:10.1371/journal.pone.0034305.t001

Cell cultures

hMSCs were maintained in alpha-MEM containing 15% FBS and antibiotics (100 units/mL penicillin G, 100 μg/mL streptomycin sulfate, and 0.25 μg/mL amphotericin B). HEK293 cells were maintained in DMEM containing 10% FBS and antibiotics. The culture medium was replaced 2 or 3 times a week. Cells were removed from the culture dish by treatment with 0.25% trypsin-0.02% EDTA in PBS and then plated on the BAM-coated dish for 30 min in culture medium. The cells attached to the BAM surface were manipulated by AFM (Fig. 1C). The cell diameter was measured from the microscopic image of the cell attached to the BAM surface.

AFM measurements

The spherical silica probe was made by bonding the silica bead onto the edge of the tipless probe with epoxy resin. hMSCs and HEK293 cells attached to the BAM-coated dishes in the medium were manipulated by AFM (Nanowizard I, JPK Instruments AG, Berlin, Germany) at room temperature. The probe indented the top of the cells up to 5 nN at 10 μm/s. The Young's modulus of the cell was calculated in accordance with the Hertz model [30]. The force-distance curve at the region up to approximately 2 nN of the cell surface indentation was fitted by JPK data processing software (JPK instruments AG) as follows:

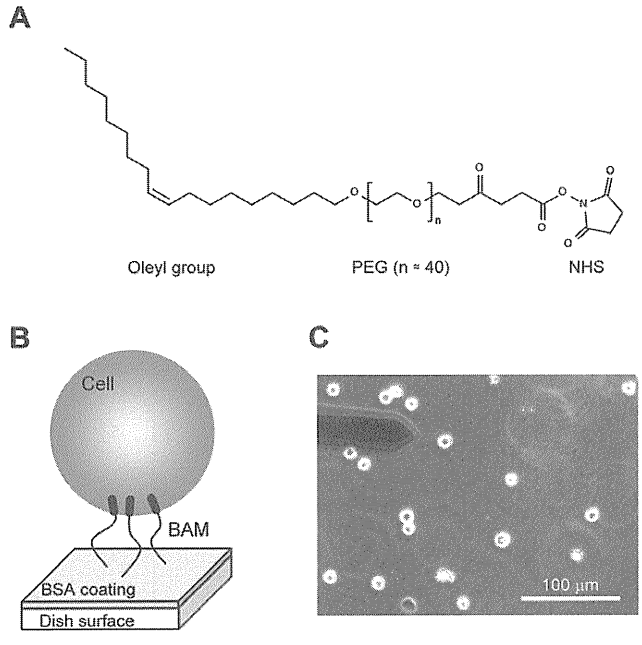

Figure 1. The Biocompatible Anchor for Membrane (BAM) system. (A) Chemical structure of BAM. It comprises an oleyl group, an NHS reactive ester group, and a hydrophilic PEG linker. (B) Diagram of the BAM-coated substrate. BAM molecules are fixed on the BSA-coated substrate via coupling with the NHS ester of BAM to the amino group of BSA. The surface oleyl group enters the plasma membrane of the cell. Then, the cell is anchored onto the BAM substrate. (C) Phase contrast micrograph of hMSCs on the BAM substrate. The floating cells were anchored to the substrate, maintaining their round shape. The left upper object is the AFM cantilever.
doi:10.1371/journal.pone.0034305.g001

$$F = \frac{4}{3}\delta^{\frac{3}{2}}\frac{E}{1-\nu^2}\sqrt{\frac{R_1 R_2}{R_1+R_2}}, \quad (1)$$

where F = force, δ = depth of indentation, R_1 = radius of spherical probe (2 μm), R_2 = radius of the cell (cell type-dependent), ν = Poisson's ratio (0.5), and E = Young's modulus (Fig. 2).

All experiments were performed using more than 100 cells, and each cell was examined at more than 25 points on the top of the cell. The median value was adopted for the Young's modulus of each cell [6]. The Young's modulus of each cell was plotted in a log histogram. The histogram was fitted by a log-normal distribution, the equation for which is as follows:

$$f(x) = y_0 + A\exp\left[-\left(\frac{\ln(x/x_0)}{w}\right)^2\right]. \quad (2)$$

The mode (x_0) and variance parameter w were obtained from the fitting.

Virtual reality system

Fig. 3A shows an image of the virtual reality system of cell indentation manipulation. An operator can feel and observe cell mechanics by moving the handle of the haptic device and touching the virtual cell object with the virtual spherical probe on the PC monitor (Fig. 3A). Virtual image updating and force calculation are performed automatically in a real-time manner with pointer locomotion. Then, the updated virtual image is transferred to the PC monitor, and the calculated force feedback is returned to the operator via the haptic device (Fig. 3). The detailed workflow, including experiments, force calculation, and virtual image update is shown in Fig. 4.

Virtual image

The cell and the probe were modeled as simplified sphere shapes and represented as spherical objects (Fig. 5A). The nucleus was set as the center of the cell object (Fig. 5B). The relative diameter of the cell in the virtual image could be changed by altering the cell diameter. The virtual space was set as 32.5 μm×32.5 μm×32.5 μm (Fig. 5B). The cell object was immobilized in the center of the virtual space, and the operator moved the probe object by manipulation with the handle of the haptic device. The cell and the probe object were only used in displaying the physical relationship in the virtual image, and thus, the cell object did not display the deformation caused by probe indentation (Fig. 5B).

Haptic representation

The motion space of the haptic handle is 101 mm× 101 mm×101 mm in real space. The virtual cell stiffness is represented by the Hertz model using the virtual depth of

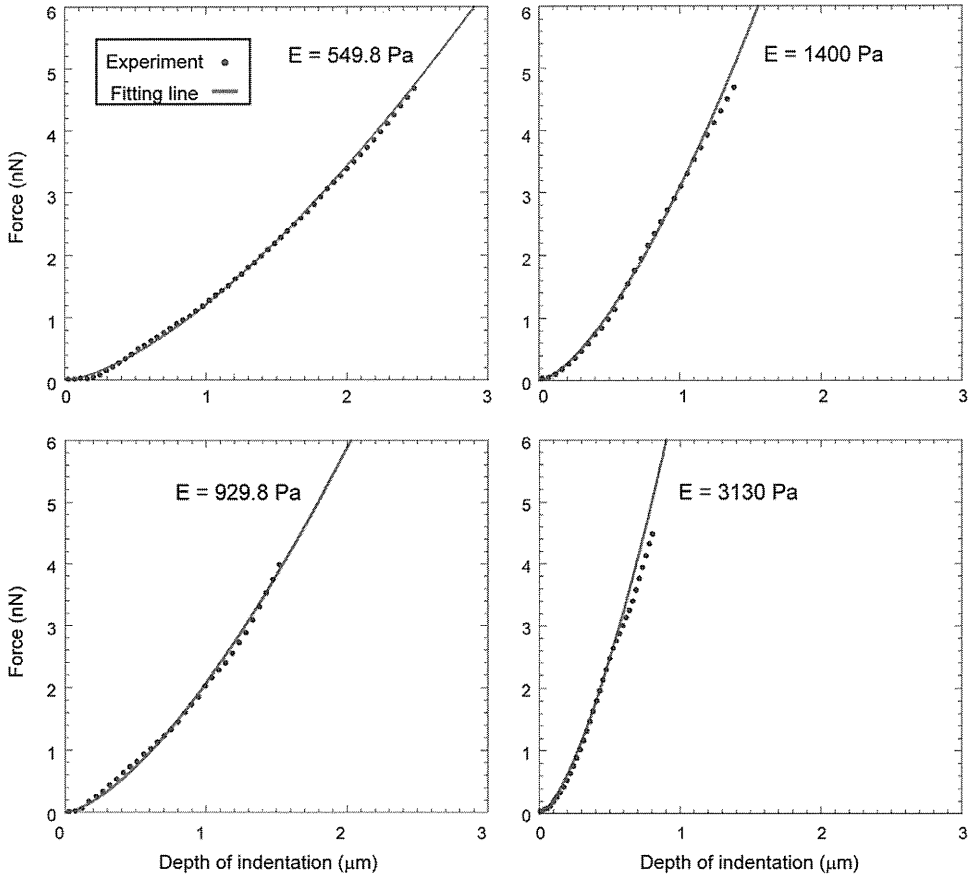

Figure 2. Typical force-distance curves obtained from the AFM indentation experiments using hMSCs. The blue points show experimental force curve lines, and the red line shows the Hertz model fitting line. The force curve at the region up to approximately 2 nN of cell surface indentation was fitted by the Hertz model. The fitting lines were well fitted to the experimental force curves in all experimental ranges.
doi:10.1371/journal.pone.0034305.g002

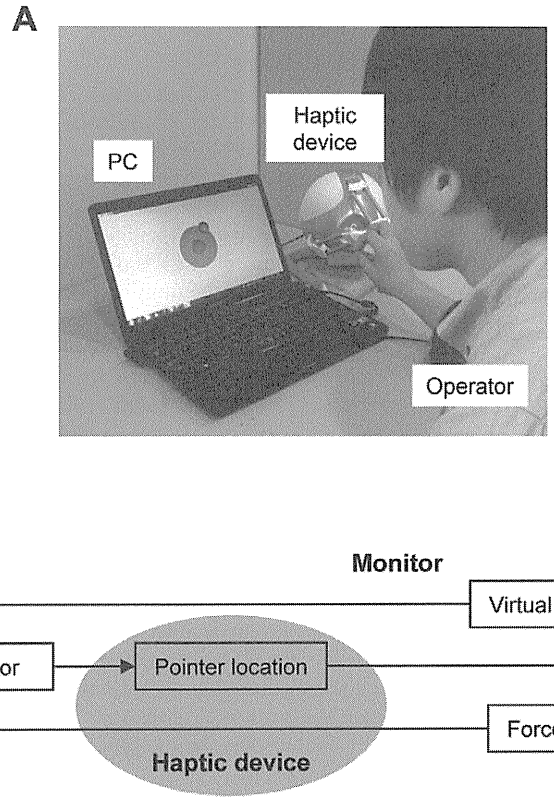

Figure 3. Virtual reality system. (A) Photograph of the system operation. The operator moves the handle of the haptic device while looking at the virtual image of the probe indentation process on the PC monitor. The operator feels the feedback force via the haptic device in conjunction with the virtual probe indentation to the cell object. (B) The relationship of the system components.
doi:10.1371/journal.pone.0034305.g003

indentation (δ_v) of the probe to the cell object (Fig. 5A). The stiffness parameters, the mode (x_0) and the variance (w) of the log-normal fitted distribution of the Young's modulus, were introduced into the simulation program, and the represented stiffness (Young's modulus, E_v) was determined with each contact of the probe and the cell objects by the Box-Muller method [31],

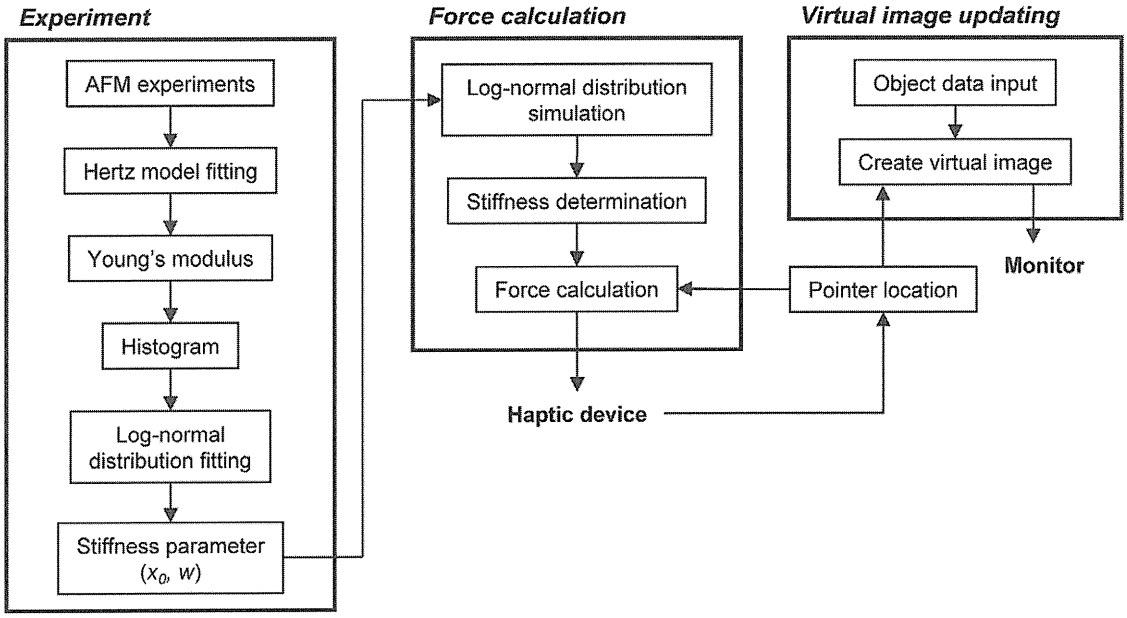

Figure 4. Detailed workflow of our system. There are 3 parts: experiment, force calculation, and virtual image updating. The stiffness parameters were previously obtained via experimentation. The obtained stiffness parameters were used in the force calculation, and the information about the cell diameter was used for virtual image updating.
doi:10.1371/journal.pone.0034305.g004

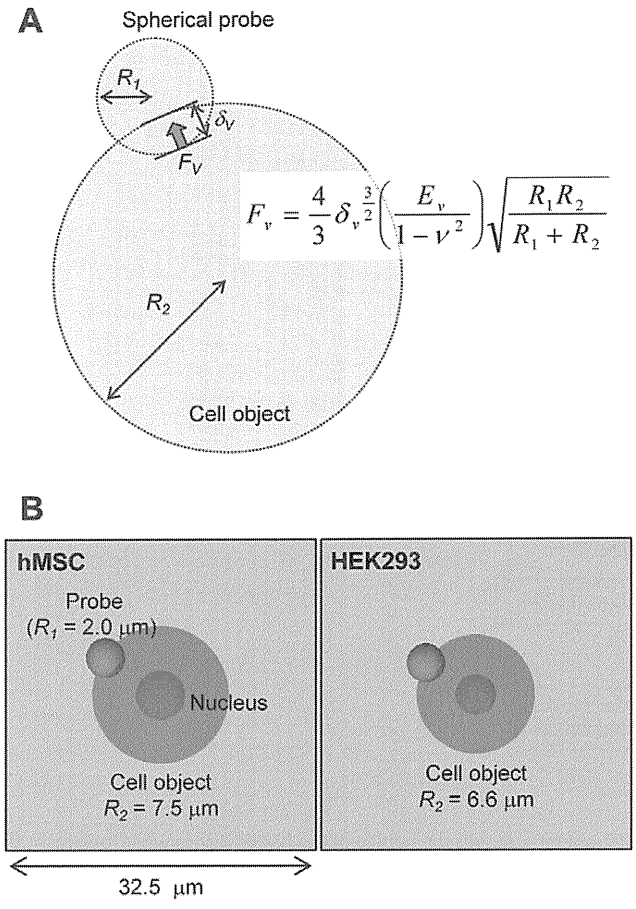

Figure 5. Virtual image of probe indentation in the cell. (A) Model of the cell object and the probe. The cell object and the probe were modeled as simplified spherical shapes. R_1 and R_2 are the radii of the probe and the cell object, respectively. δ_V is the indentation depth of the probe into the cell object. The push back force (F_V) to the probe from the cell was calculated by the Hertz model using δ_V and the determined E_V. (B) The representative virtual images. The left image represents hMSCs, and the right image represents HEK293 cells. The cell radii (R_2) of hMSCs and HEK293 cells were 7.5 and 6.6 μm, respectively. The blue nucleus is fixed in the center of the cell object. The virtual space is 32.5 μm×32.5 μm×32.5 μm. The probe can be moved freely in the virtual space.
doi:10.1371/journal.pone.0034305.g005

which creates log-normal distribution-dependent random numbers by using these stiffness parameters. The details are as follows. The 2 independent random variables, α and β, are uniformly distributed in the interval (0, 1). The random variable N with a normal distribution of standard deviation 1 is given as

$$N = (-2\ln\alpha)^{1/2}\sin(2\pi\beta). \quad (3)$$

Then, using N, the E_v is given as

$$E_v = \exp\left[N \cdot w/\sqrt{2} + \ln(x_0)\right]. \quad (4)$$

Finally, the represented F_v, which was determined by a Hertz model equation with the determined E_v and δ_v, is sent to the haptic device in real time.

Results and Discussion

Experimental cell stiffness

Many types of cells are used for cell culture. Thus, innumerable cell types were available for use in evaluating the mechanical properties of a cell by the virtual reality system. The mechanical properties of a cell are represented using the haptic device, and the physical relationship between the cell and the probe is represented on the PC monitor by displaying these findings virtually. On the other hand, cultured cell morphology is different in each cell and each cell type. Thus, to display the morphology of all types of cells easily, we represented the mechanical properties in the floating cell state in our virtual reality system. The morphology of the floating cell is almost spherical irrespective of cell types, and it is easy to display the spherical object by using a PC.

The mechanical properties of surface-immoliblized nonadherent leukocytes using AFM have been reported earlier [10,32]. Here, we used the BAM substrate to determine the mechanical properties of floating cells by AFM. BAM contains a cytoplasmic anchoring oleyl group, a hydrophilic PEG domain, and an NHS reactive ester group [29]. The BAM substrate was constructed from the BSA substrate by coupling the NHS ester of the BAM molecule to the amino group of BSA (Fig. 1B). The trypsinized floating cell attached to the BAM substrate spontaneously (Fig. 1C). The attached cell was anchored to the substrate tightly, and it was not removed from the surface by swinging. Then, we measured cell stiffness in the floating state by the probe indentation method using AFM (Fig. 1C).

Fig. 2 shows the typical force curves and their Hertz model fitting curves in hMSC experiments. Although the adaptation range of the Hertz model is limited by the small indentation depth of the probe, the fitting curves were well fitted in the entire experimental indentation range (Fig. 2). The reasons for the good fitting are the isotropy of the floating cell on the BAM substrate and the simple indentation process of the 2 spherical objects (spherical cell and probe). An adhered cell has anisotropic membrane tension and actin fibers [33]. Furthermore, the shape and the structure of an adhered cell are complicated and varied. These elements complicate the indentation process of the probe to the cell surface. In this study, the represented force F_v corresponding to the indentation depth of the probe was calculated with the Hertz model equation (Fig. 5).

Fig. 6 shows histograms of the Young's modulus of hMSCs and HEK293 cells. The distributions of Young's modulus of these cells were clearly different, and the Young's modulus of hMSCs was higher than that of HEK293 cells (Fig. 6). The average cell diameters of hMSCs and HEK293 cells were 15.0±3.0 and 13.2±2.2 μm, respectively. The Young's modulus of each cell was distributed broadly and in each range was extended by single digits for both cell types (Fig. 6). Then, each Young's modulus distribution was fitted by a log-normal pattern. The mode values (x_0) of the Young's modulus of hMSCs and HEK293 cells were 2050 and 410 Pa, respectively. The variance parameters w for these cells were 0.733 and 0.757, respectively. Therefore, the breadth of the distribution of Young's modulus was similar in both cells in the floating state. It is, however, unclear whether the breadth of the Young's modulus distribution of the floating cell is almost identical.

In contrast, the distribution of the Young's modulus of a single cell was narrower than that of the same cell type (Fig. 7). The mode value (x_0) and variance parameter w of the log-normal fitted distribution of Young's modulus of a single hMSC were 1950 Pa and 0.394 respectively. In this study, we developed a virtual reality system to represent the mechanical properties (Young's modulus and its variance) of each cell type.

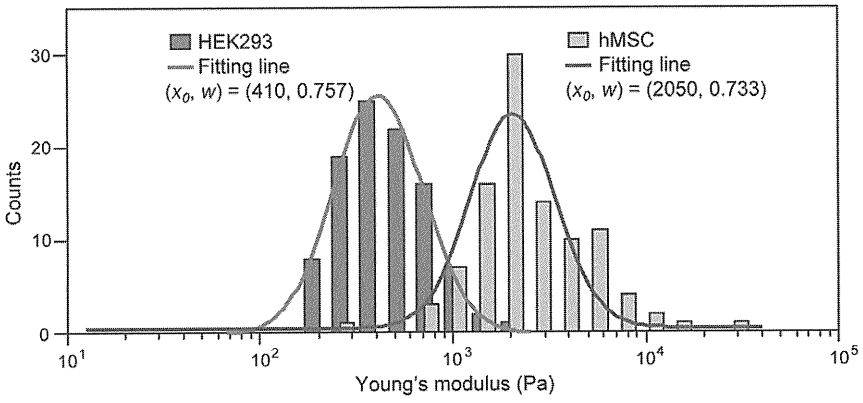

Figure 6. Histogram of the Young's modulus distributions of hMSCs and HEK293 cells. Each histogram consists of the Young's modulus data of 100 cells. Each histogram is fitted with a log-normal pattern (fitted line). The fitting stiffness parameters, mode value x_0, and variance parameter w are shown.
doi:10.1371/journal.pone.0034305.g006

Virtual reality system

In the virtual reality system, to represent the aforementioned mechanical properties of the cell, we adopted the Box-Muller method for determining Young's modulus, which creates log-normal distribution-dependent random numbers [31]. Fig. 8 shows the distribution of the simulated values by the Box-Muller method using the parameters of the mechanical properties of hMSCs. Using this method, we succeeded in demonstrating the log-normal distribution of the mechanical properties of hMSCs. The represented Young's modulus value was calculated for each touching event of the probe surface and the cell object (Fig. 5). The haptic presentation force (F_v) was calculated regarding to the indentation depth (δ_v) and the determined Young's modulus value (E_v) (Fig. 5).

In presenting the calculated force (F_v) via the haptic device, its scale became controversial in real space. The scale of the calculated force (F_v) was almost in the range of pN to nN, and the value was too small to present the force in the haptic device. Even if considering the scale conversion ratio of real space to virtual space (101 mm in real space to 32.5 μm in virtual space), the scale of the force was almost in the range of μN (approximately 1×10^5-fold more than the calculated F_d). Therefore, we prioritized the recognition of the relation and difference of the mechanical properties of each cell type in real space rather than presenting the real value. The presented force was enlarged 5×10^{10}-fold in real space.

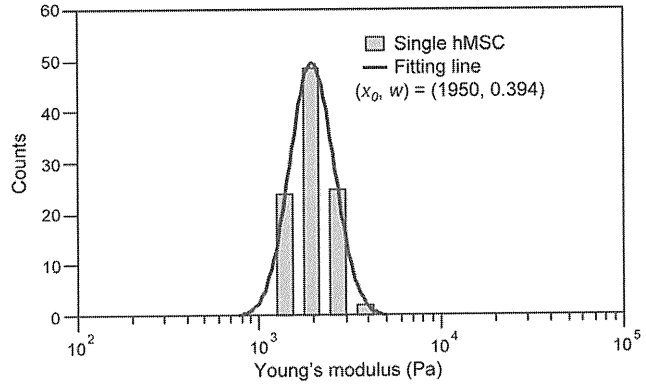

Figure 7. Histogram of the Young's modulus distribution of a single hMSC measurement. A single hMSC was measured 100 times. The histogram was fitted with a log-normal pattern.
doi:10.1371/journal.pone.0034305.g007

The spherical probe was subjected to drag force and buoyant force from the water and gravity in the background. The viscous drag F_d for the spherical probe ($r = 2$ μm; $v = 10$ μm/s) is 0.337 pN at 25°C (Text S1). The gravity (F_g) for the silica probe ($\rho = 2200$ kg/m^3) is 0.723 pN, and the buoyant force (F_b) is 0.329 pN (Text S1). These forces are much smaller than the F_v, and thus, we did not account for their effects in our study.

On our PC, the performance of which is shown in Table 1, the time delay from the input to the output of the haptic device was ~1 ms. The time interval required to calculate each Young's modulus at the contact of the probe and the cell surface was nearly 0 ms. These time delays (total, ~1 ms) were sufficiently fast for the time resolution of human haptic recognition (approximately several 100 Hz) [34]. Therefore, our virtual reality system succeeded in representing the mechanical properties of a cell in real time.

The supplemental video S1 shows the actual situation of the system operation. The depth of each probe indentation with constant force varied in each cell touching, and occasionally virtual cell showed very high or low stiffness. Moreover, the virtual hMSC and HEK293 cell apparently showed different stiffness. These differences among the same type of cells or between each cell type were clearly understood by using this virtual reality system.

Our system consisted of a PC, including a monitor, and the haptic device. The haptic device (Falcon), which is offered commercially as a PC game controller, is a low-budget device, and our PC is a common type. Moreover, our system does not require any special software or high performance computer due to excluding the display of cell deformation. Thus, our developed virtual reality system can be easily created in any laboratory and for any exhibition, and the only necessary information is the mechanical properties of a cell, i.e., the mode and variance of the distribution of the Young's modulus of the cell. These mechanical properties can be gathered in a database. In short, using our system, anyone can perceive the mechanical properties of any existing cell type. In the future, we expect that the mechanical properties of cells will become tangible features for sharing and communication with many people.

Conclusions

This study introduced a new simple display system that presented the mechanical properties and their dispersion of each

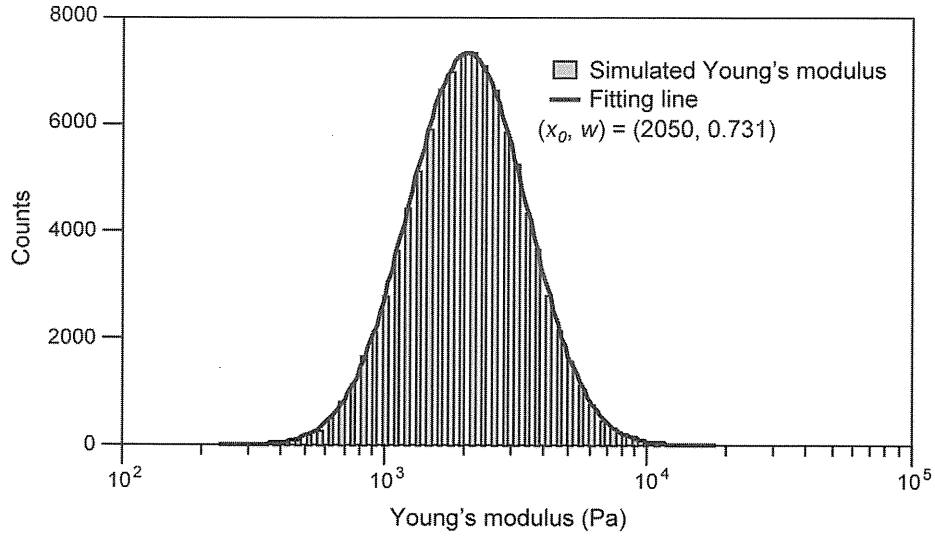

Figure 8. Histogram of the simulated Young's modulus distribution obtained using the Box-Muller method. The simulation was trialed 100,000 times using hMSC stiffness parameters. The histogram was fitted with a log-normal pattern. The represented Young's modulus (E_v) was in accordance with the simulated value.
doi:10.1371/journal.pone.0034305.g008

cell type as measured by AFM. The system enabled presentation of the mechanical properties of various floating cell types by simulating the AFM nanoindentation experiments. It is indeed difficult to imagine or viscerally understand the mechanical properties of cells and their cell type-specific differences, also the mechanical interaction between adjacent cells or between a cell and its physical microenvironment. Therefore, we are scarcely able to communicate or share the mechanical properties of cells with others. According to our developed mechanical information display system by using virtual reality technology, we can not only recognize the mechanical properties of each cell but also share them. This will make the mechanical information of cells an intelligible character for researchers, including biochemists, cell biologists, and developmental biologists, thereby stimulating the research field of cell mechanics.

Supporting Information

Text S1 The physical forces for the AFM probe in water.
(PDF)

Video S1 Video imaging of the system operation. The first part of the video shows the situation of the operation for virtual hMSC, and the last part shows the operation for virtual HEK293 cell. Apparently, the lengths of the probe indentation vary between virtual hMSC and HEK293 cell.
(WMV)

Author Contributions

Conceived and designed the experiments: YS TK. Performed the experiments: YS. Analyzed the data: YS. Contributed reagents/materials/analysis tools: SMAH SY. Wrote the paper: YS TK SMAH. Developed the system: YS. Final approval of manuscript: TK SY JM.

References

1. Cross SE, Jin YS, Rao J, Gimzewski JK (2007) Nanomechanical analysis of cells from cancer patients. Nat Nanotechnol 2: 780–783.
2. Nash GB, O'Brien E, Gordon-Smith EC, Dormandy JA (1989) Abnormalities in the mechanical properties of red blood cells caused by Plasmodium falciparum. Blood 74: 855–861.
3. Eiraku M, Takata N, Ishibashi H, Kawada M, Sakakura E, et al. (2011) Self-organizing optic-cup morphogenesis in three-dimensional culture. Nature 472: 51–56.
4. Sugitate T, Kihara T, Liu X-Y, Miyake J (2009) Mechanical role of the nucleus in a cell in terms of elastic modulus. Current Applied Physics 9: e291–e293.
5. Maloney JM, Nikova D, Lautenschlager F, Clarke E, Langer R, et al. (2010) Mesenchymal stem cell mechanics from the attached to the suspended state. Biophys J 99: 2479–2487.
6. Kihara T, Haghparast SM, Shimizu Y, Yuba S, Miyake J (2011) Physical properties of mesenchymal stem cells are coordinated by the perinuclear actin cap. Biochem Biophys Res Commun 409: 1–6.
7. Collinsworth AM, Zhang S, Kraus WE, Truskey GA (2002) Apparent elastic modulus and hysteresis of skeletal muscle cells throughout differentiation. Am J Physiol Cell Physiol 283: C1219–1227.
8. Trickey WR, Vail TP, Guilak F (2004) The role of the cytoskeleton in the viscoelastic properties of human articular chondrocytes. J Orthop Res 22: 131–139.
9. Titushkin I, Cho M (2006) Distinct membrane mechanical properties of human mesenchymal stem cells determined using laser optical tweezers. Biophys J 90: 2582–2591.
10. Kagiwada H, Nakamura C, Kihara T, Kamiishi H, Kawano K, et al. (2010) The mechanical properties of a cell, as determined by its actin cytoskeleton, are important for nanoneedle insertion into a living cell. Cytoskeleton (Hoboken) 67: 496–503.
11. Pollard TD, Cooper JA (2009) Actin, a central player in cell shape and movement. Science 326: 1208–1212.
12. Fletcher DA, Mullins RD (2010) Cell mechanics and the cytoskeleton. Nature 463: 485–492.
13. Olson EN, Nordheim A (2010) Linking actin dynamics and gene transcription to drive cellular motile functions. Nat Rev Mol Cell Biol 11: 353–365.
14. Dai J, Sheetz MP (1995) Mechanical properties of neuronal growth cone membranes studied by tether formation with laser optical tweezers. Biophys J 68: 988–996.
15. Van Vliet KJ, Bao G, Suresh S (2003) The biomechanics toolbox: experimental approaches for living cells and biomolecules. Acta Materialia 51: 5881–5905.
16. Huang H, Kamm RD, Lee RT (2004) Cell mechanics and mechanotransduction: pathways, probes, and physiology. Am J Physiol Cell Physiol 287: C1–11.
17. Matzke R, Jacobson K, Radmacher M (2001) Direct, high-resolution measurement of furrow stiffening during division of adherent cells. Nat Cell Biol 3: 607–610.
18. Costa KD (2006) Imaging and probing cell mechanical properties with the atomic force microscope. Methods Mol Biol 319: 331–361.
19. Mathur AB, Truskey GA, Reichert WM (2000) Atomic force and total internal reflection fluorescence microscopy for the study of force transmission in endothelial cells. Biophys J 78: 1725–1735.
20. Nagayama M, Haga H, Kawabata K (2001) Drastic change of local stiffness distribution correlating to cell migration in living fibroblasts. Cell Motil Cytoskeleton 50: 173–179.

21. Bro-Nielsen M (1998) Finite element modeling in surgery simulation. Proceedings of the IEEE 86: 490–503.
22. Cotin S, Delingette H, Ayache N (1999) Real-time elastic deformations of soft tissues for surgery simulation. Ieee Transactions on Visualization and Computer Graphics 5: 62–73.
23. Fager PJ, von Wowern P (2004) The use of haptics in medical applications. Int J Med Robot 1: 36–42.
24. Kuroda Y, Nakao M, Kuroda T, Oyama H, Komori M (2005) Interaction model between elastic objects for haptic feedback considering collisions of soft tissue. Comput Methods Programs Biomed 80: 216–224.
25. Choi C, Kim J, Han H, Ahn B, Kim J (2009) Graphic and haptic modelling of the oesophagus for VR-based medical simulation. International Journal of Medical Robotics and Computer Assisted Surgery 5: 257–266.
26. Ladjal H, Hanus JL, Pillarisetti A, Keefer C, Ferreira A, et al. (2009) Atomic force microscopy-based single-cell indentation: Experimentation and finite element simulation. Proc IEEE Int Conf Intell Robots Syst Oct 11–15 2009. pp 1326–1332.
27. Ladjal H, Hanus JL, Pillarisetti A, Keefer C, Ferreira A, et al. (2010) Reality-Based Real-Time Cell Indentation Simulator. IEEE/ASME Transactions on Mechatronics 15: 1–12.
28. Kotobuki N, Hirose M, Machida H, Katou Y, Muraki K, et al. (2005) Viability and osteogenic potential of cryopreserved human bone marrow-derived mesenchymal cells. Tissue Eng 11: 663–673.
29. Kato K, Umezawa K, Funeriu DP, Miyake M, Miyake J, et al. (2003) Immobilized culture of nonadherent cells on an oleyl poly(ethylene glycol) ether-modified surface. Biotechniques 35: 1014–1018, 1020–1011.
30. Hertz H (1881) Über die berührung fester elastischer Körper. J reine und angewandte Mathematik 92: 156–171.
31. Box GEP, Muller ME (1958) A note on the generation of random normal deviates. Ann Math Statist 29: 610–611.
32. Lulevich V, Zink T, Chen HY, Liu FT, Liu GY (2006) Cell mechanics using atomic force microscopy-based single-cell compression. Langmuir 22: 8151–8155.
33. Fouchard J, Mitrossilis D, Asnacios A (2011) Acto-myosin based response to stiffness and rigidity sensing. Cell Adh Migr 5: 16–19.
34. Burdea GC, Coiffet P (2003) Viurtual Reality Technology Wiley-IEEE Press.

JOURNAL OF TISSUE ENGINEERING AND REGENERATIVE MEDICINE
J Tissue Eng Regen Med (2011).
Published online in Wiley Online Library (wileyonlinelibrary.com) **DOI:** 10.1002/term.427

RESEARCH ARTICLE

Bone morphogenetic protein-2 in biodegradable gelatin and β-tricalcium phosphate sponges enhances the *in vivo* bone-forming capability of bone marrow mesenchymal stem cells

Mika Tadokoro[1], Asako Matsushima[1], Noriko Kotobuki[1], Motohiro Hirose[2], Yu Kimura[3], Yasuhiko Tabata[3], Koji Hattori[1] and Hajime Ohgushi[1]*

[1]*Health Research Institute, National Institute of Advanced Industrial Science and Technology (AIST), 3-11-46 Nakoji, Amagasaki, Hyogo 661-0974, Japan*
[2]*Human Technology Research Institute, National Institute of Advanced Industrial Science and Technology (AIST), 1-1-1 Higashi, Tsukuba, Ibaraki 305-8566, Japan*
[3]*Department of Biomaterials, Field of Tissue Engineering, Institute for Frontier Medical Sciences, Kyoto University, 53 Kawara-cho Shogoin, Sakyo-ku, Kyoto 606-8507, Japan*

Abstract

Bone marrow mesenchymal stem cells (MSCs) have been used for bone tissue engineering due to their osteogenic differentiation capability, but their application is controversial. To enhance their capability, we prepared biodegradable gelatin sponges incorporating β-tricalcium phosphate ceramics (GT sponge), which has been shown to possess excellent controlled drug-release properties. The GT sponge was used as a carrier for both rat MSCs and bone morphogenetic protein-2 (BMP-2) and osteogenic differentiation was assessed by subcutaneous implantation of four different kinds of implants, i.e. GT-alone, MSC–GT composites, BMP–GT composites and BMP–GT composites supplemented with MSCs (BMP–MSC–GT) in rats. Two weeks after implantation, histological sections showed new bone formation in the peripheral parts of the BMP–GT and in almost the total volume of the BMP–MSC–GT implants. After 4 weeks, histology as well as microCT analyses demonstrated extensive bone formation in BMP–MSC–GT implants. Gene expression and biochemical analyses of both alkaline phosphatase and bone-specific osteocalcin confirmed the histological findings. These results indicate that the combination of MSCs, GT and BMP synergistically enhances osteogenic capability and provides a rational basis for their clinical application in bone reconstruction. Copyright © 2011 John Wiley & Sons, Ltd.

Received 21 July 2010; Accepted 13 March 2011

Keywords **gelatin; bone morphogenetic protein-2 (BMP-2); controlled drug release; mesenchymal stem cell; osteogenesis**

1. Introduction

Bone defects have been clinically treated by implantation of various bone grafts or artificial bone graft substitutes. Autogenous bone is the gold standard for bone grafts because it has many advantages, including the absence of infections and biocompatibility, as well as osteoconductive and osteoinductive properties mediated via growth factors in the bone matrix. However, there are also many problems, such as quantitative limitations of the grafts and the inevitable invasion of normal tissues to harvest the bone graft. To avoid these problems, artificial bone substitutes, such as hydroxyapatite (HA) and β-tricalcium phosphate (β-TCP) ceramics, can be combined with collagen or other proteins and have

Correspondence to: Hajime Ohgushi, Health Research Institute, National Institute of Advanced Industrial Science and Technology (AIST), 3-11-46 Nakoji, Amagasaki, Hyogo 661-0974, Japan. E-mail: hajime-ohgushi@aist.go.jp

been used in clinical situations (LeGeros, 2008). Calcium phosphate ceramics are biocompatible, osteoconductive and bioactive, but it has been hard to conclusively show whether they have osteoinductive capability (Giannoudis *et al.*, 2005; Yoshikawa *et al.*, 2005).

It is now recognized that bone marrow is a major reservoir of mesenchymal stem cells (MSCs), which can differentiate not only into osteoblasts and chondrocytes, but also into other types of cells, such as hepatocytes, neural cells and stem cells that support haematopoiesis. MSCs have been regarded as the most reliable cell source for the purpose of bone tissue engineering after their combination with various scaffolds, including ceramics. We previously reported clinical application of autologous MSCs derived from patients' bone marrow for the treatment of bone diseases (Kawate *et al.*, 2006; Morishita *et al.*, 2006; Ohgushi *et al.*, 2004, 2005). However, in some cases, the osteogenic potential of the MSCs was not high enough for a good clinical outcome. If the potential could be increased by the addition of growth factors, promising results and an early start to rehabilitation could be achieved.

Growth factors such as bone morphogenetic proteins (BMPs), transforming growth factor-β (TGF-β) and basic fibroblast growth factor (bFGF) have been used to enhance bone regeneration. Among them, BMPs are reported to be useful in healing bone defects because of their osteoinductive properties. In particular, BMP-2 has been well characterized and is a very potent osteoinductive growth factor (Ikeuchi *et al.*, 2002; Reddi and Cunningham, 1993; Tabata, 2008, 2009; Zegzula *et al.*, 1997). However, the administration of BMP-2 in orthopaedic applications is restricted, due to its short biological half-life and localized actions (Ruhe *et al.*, 2006). To overcome these problems, incorporation of BMP-2 into biomaterials is necessary for its effective delivery at the *in vivo* implanted target site.

We previously developed biodegradable gelatin sponges incorporating β-TCP (GT) for the controlled release of BMP-2 (Takahashi *et al.*, 2005a, b). The controlled release of growth factors from gelatin results from the enzymatic degradation of gelatin, and the extent of gelatin crosslinking affects its degradation (Tabata *et al.*, 1999). Many studies have shown that GT sponge is an excellent carrier for various kinds of growth factors, but the efficacy of the sponge as a BMP-2 carrier, particularly for *in vivo* osteogenic potential of MSCs, is not clear. Here we show that the osteogenic potential of MSCs was accelerated by the high activity of BMP-2 incorporated into GT sponge, and therefore the combination of GT sponge, BMP-2 and MSCs could be used as an ideal approach for the purpose of bone tissue engineering.

2. Materials and methods

2.1. Preparation of mesenchymal stem cells

MSCs were derived from the femora of 7 week-old, male Fischer 344 rats, as previously described (Maniatopoulos *et al.*, 1988; Ohgushi *et al.*, 1996). The bone marrow was flushed out using 10 ml culture medium expelled from a syringe through a 21-gauge needle. The bone marrow was cultured in T-75 flasks containing 15 ml culture medium, consisting of minimum essential medium (MEM; Nacalai Tesque, Kyoto, Japan) with 15% fetal bovine serum (FBS; JRH Bioscience, KS, USA), 100 U/ml penicillin, 0.1 mg/ml streptomycin and 0.25 μg/ml amphotericin B (Nacalai Tesque). To remove non-adherent cells, the medium was changed after 2 days and subsequently renewed three times/week. Adherent cells were expanded as monolayer cultures in a humidified atmosphere of 5% CO_2 and 95% air at 37 °C. After 7 days of cultivation, the confluent cells were dissociated with 0.25% trypsin–EDTA and used for all experiments. To confirm the osteogenic capability of BMP-2 to differentiate MSCs into osteoblasts, MSCs were cultured with different amounts of BMP-2.

2.2. Preparation of gelatin-β-TCP sponges incorporating BMP-2

The manufacturing procedure of gelatin-β-TCP sponges used in this study was described previously (Takahashi *et al.*, 2005a, 2005b). In brief, an aqueous solution of gelatin and 50 wt% β-TCP granules (average diameter 2 μm; Taihei Chemical Industries, Nara, Japan) were mixed with a homogenizer. After addition of aqueous glutaraldehyde solution, the mixed solution was cast into a polypropylene dish and left at 4 °C for 12 h to allow gelatin cross-linking. Cross-linked gelatin sponges with β-TCP were then placed into aqueous glycine solution to block the residual aldehyde groups of glutaraldehyde. After washing with double-distilled water, the sponges were freeze-dried and cut into pieces 5 mm in diameter × 2 mm thick.

Commercially available gelatin sponge (Spongel®; Astellas Pharma, Tokyo, Japan) was used as a control for the GT sponges. The gelatin sponges were stamped out using a punch in a disk 5 0 mm in diameter × 2 mm thick.

BMP-2 was dissolved to make a concentration of 0.25 μg/μl in Milli-Q water. To incorporate BMP-2, 20 μl BMP-2 solution was impregnated into the gelatin–β-TCP sponges, which were freeze-dried. Gelatin sponges incorporating BMP-2 were prepared similarly as controls.

2.3. Implantation of gelatin–β-TCP sponges incorporating BMP-2

As shown in Table 1, we prepared eight experimental groups of implants as follows: gelatin–β-TCP sponge

Table 1. Number of implants per experimental group

Implants*				
GT alone	MSC-GT composites	BMP-GT composites	BMP-MSC-GT composites	Harvest time after implantation (weeks)
15	15	15	15	2
15	15	15	15	4
Implants*				
Sp alone	MSC-Sp composites	BMP-Sp composite	BMP-MSC-Sp composites	Harvest time after implantation (weeks)
15	15	15	15	2
15	15	15	15	4

*Total number of implants in each group was 15. Fifteen samples were used for μ-CT ($n = 5$), histological analysis ($n = 3$), biochemical analysis ($n = 4$) and gene expression ($n = 3$) after implantation.

alone (GT); GT with MSCs (MSC–GT); GT with BMP-2 (BMP–GT); GT with MSCs and BMP-2 (BMP–MSC–GT); gelatin sponge alone (Sp); Sp with MSCs (MSC–Sp); Sp with BMP-2 (BMP–Sp); Sp with MSCs and BMP-2 (BMP–MSC–Sp). The MSCs were suspended in the culture medium at a concentration of 1×10^7/ml. Twenty μl (2×10^5 cells/sample) of the cell suspensions were loaded into the sponges (for the groups MSC–GT and MSC–Sp) or the sponges combined with BMP-2 (for the groups BMP–MSC–GT and BMP–MSC–Sp) and were incubated at 37 °C for 1 h before implantation. The number of implants is summarized in Table 1. The samples were implanted subcutaneously into Fischer 344 rats. Four subcutaneous pockets were created on each side of the rat's back; therefore, one sample from each of the eight groups was implanted into a separate pockets. The total number of recipient rats per time period was 10; consequently, each group received 15 implants. The implants were harvested at 2 and 4 weeks after implantation and analysed histologically and biochemically.

2.4. MicroCT analysis

After implantation, five implants were harvested and fixed in buffered formalin for 1 day. The implants were scanned using micro-computed tomography (μCT; Hitachi Medical, Tokyo, Japan) for visualization of new bone. μCT was performed on fixed samples at 55 kV and 150 μA. The analytical conditions were: precision mode, ×10.5 magnification with an image intensifier field of 1.8 inches, total of 256 sagittal sections scanned. The intensity of newly formed bone was defined as the same level intensity of the osseous tissue (2165–2550 LUT). Total volume and the number of bone detections were measured using the software package TRI3D-BON (Ratoc System Engineering, Tokyo, Japan) according to the methods we previously reported (Nishikawa *et al.*, 2004).

Table 2. Quantitative real-time PCR primers

Alkaline phosphatase (ALP)
Forward, 5′-GAC AAG AAG CCC TTC ACA GC-3′
Reverse, 5′-ACT GGG CCT GGT AGT TGT TG-3′
Osteocalcin (OCN)
Forward, 5′-AAG CCC AGC GAC TCT GAG TC-3′
Reverse, 5′-GCT CCA AGT CCA TTG TTG AGG-3′
Glyceraldehyde-3-phosphate dehydrogenase (GAPDH)
Forward, 5′-AAC GAC CCC TTC ATT GAC CTC-3′
Reverse, 5′-CCT TGA CTG TGC CGT TGA ACT-3′

2.5. Histological analysis

Three implants of each group were fixed using 10% neutral buffered formalin, decalcified, dehydrated and embedded in paraffin for histological analysis. Sections were stained with haematoxylin and eosin (H&E).

2.6. Gene expression and biochemical analysis of implants

Two and 4 weeks after implantation, total RNA was extracted from the implants using TRIzol reagent (Invitrogen, CA, USA) according to the manufacturer's instructions. Then cDNA templates were synthesized using RevaTra Ace cDNA kit (Totobo, Osaka, Japan), following the manufacturer's instructions. Samples incubated in the absence of reverse transcriptase were used as controls. Gene expression levels of alkaline phosphatase (ALP) and osteocalcin were measured using a quantitative real-time PCR cycler (qPCR; iCycler iQ system, BioRad, CA, USA). The QuantiTect SYBER Green PCR (Qiagen) was used according to the manufacturer's instructions. Primer sequences are listed in Table 2. In all experiments, appropriate negative controls without template were subjected to the same procedure to detect DNA contamination or carry-over. The data were standardized to the gene expression level of the endogenous control,

glyceraldehyde-3-phosphate dehydrogenase (*GAPDH*). This allowed for differences in the amount of total RNA added to each reaction to be taken into account.

For biochemical analysis, the ALP activity and osteocalcin contents of the implants were measured at 2 and 4 weeks post-implantation. After washing with PBS, the implants were homogenized in 1 ml 0.2% Triton-X 100 solution and sonicated for 5 min. After centrifuging, the supernatant was assayed for ALP activity as described above. To measure osteocalcin in the implants, osteocalcin was extracted from the sediment of the Triton-X 100 extract by decalcification, using a 20% formic acid solution for <24 h at 4 °C. After desalting, using a prepacked Sephadex G-25 column (NAP-5 column; GE Healthcare UK, Buckinghamshire, UK), the eluted protein fraction was lyophilized and subjected to a Rat Osteocalcin EIA Kit (Biomedical Technologies, MA, USA) according to the manufacturer's instructions.

2.7. Statistics

For multiple comparisons, the groups were compared by non-parametric Kruskal–Wallis test. When significant variance was demonstrated, differences between individual groups were determined using the Mann–Whitney U-test with Bonferroni correction. In all analysis, the significance level was set at $p < 0.05$.

3. Results

3.1. MicroCT analysis

GT sponges implanted subcutaneously into the backs of rats were retrieved for μCT and histological analysis 2 and 4 weeks after implantation. Typical μCT images of sagittal sections of the implants are shown in Figure 1. The GT sponges had a low intensity before implantation. μCT images of some implant groups using GT sponges showed an increase in intensity at 2 weeks. Four weeks after implantation, the images of both the BMP–GT and BMP–MSC–GT implants showed high-intensity (white) areas. In the implants using gelatin sponge (Sp), a high-intensity area was only observed in the BMP–MSC–Sp group 2 weeks after implantation.

As described in our previous report (Nishikawa *et al.*, 2004), we could define the high-intensity areas as new bone formation. The average volumes of bone in the GT sponge implants were 0.0043 ± 0.0010 mm^3 in GT, 0.0057 ± 0.0503 mm^3 in MSC–GT, 0.16010 ± 0.1142 mm^3 in BMP–GT, and 5.8690 ± 1.5267 mm^3 in BMP–MSC–GT composites, respectively. The numbers of detections of bone were 0 in GT, 1 in MSC–GT, 4 in BMP–GT and 5 in BMP–MSC–GT composite, respectively (Figure 2A, C). The number of bone detections in the BMP–MSC–Sp group was only one out of five samples 2 weeks after implantation. After 4 weeks, we could not detect newly formed bone in any implants of the Sp, MSC–Sp, BMP–Sp or BMP–MSC–Sp groups. We confirmed that control samples (GT-alone) showed a background level of X-ray absorbance (Figure 2B). β-TCP granules (2 μm average diameter) incorporated sponge did not appear in 3D imaging because the μCT had a resolution of about 5 μm.

3.2. Histological analysis

Histological evaluation confirmed that the high-intensity areas seen in the μCT scan corresponded to areas of newly formed bone. Two weeks after implantation, histological sections showed new bone formation with osteoblasts and osteocytes in both BMP–GT and BMP–MSC–GT implants (Figure 3A), although new bone formation was only observed in the peripheral areas of the BMP–GT implants, while bone was seen throughout the BMP–MSC–GT implants (Figure 3B). Newly formed bone was also detected in the BMP–MSC–Sp implants but not in Sp-alone, BMP–Sp or MSC–Sp implants 2 weeks after implantation. After 4 weeks, more extensive bone formation was observed in the BMP–GT and BMP–MSC–GT implants (Figure 3A, B). The bone tissue in both BMP–GT and BMP–MSC–GT implants showed many osteocytes together with abundant extracellular bone matrix. Some areas of the BMP–MSC–GT implants also showed the existence of bone marrow-like tissue. As described above, none of the Sp implants were detected in the implanted areas and therefore could not be harvested at the 4-week time point.

3.3. Alkaline phosphatase and osteocalcin expression of implants

The gene expression profiles of alkaline phosphatase (ALP) and osteocalcin in the implants were analysed by qPCR (Figure 4). The expression levels of *ALP* mRNA in the BMP–MSC–GT group were higher than in the other GT groups after 2 weeks. After 4 weeks, the expression levels of *ALP* mRNA in the MSC–GT, BMP–GT and BMP–MSC–GT groups increased. The expression levels of *osteocalcin* mRNA in the BMP–MSC–GT group were also higher than those of the other GT groups.

Biochemical measurement of ALP activity was significantly higher in BMP–MSC–GT than in the other GT groups at 2 weeks, but after 4 weeks the ALP activity levels decreased (Figure 4B). However, both the BMP–GT and BMP–MSC–GT groups had high ALP activity levels compared with the GT-alone and MSC–GT groups. ALP activity in the Sp implants was as low as the GT-alone group (data not shown). High osteocalcin levels were detected in the BMP–MSC–GT group 2 weeks after implantation and this increased five-fold after 4 weeks. The BMP–GT group also showed a similar increase between 2 and 4 weeks. The highest content was seen in the BMP–MSC–GT 4 weeks after implantation. These findings correlated well with the histological sections,

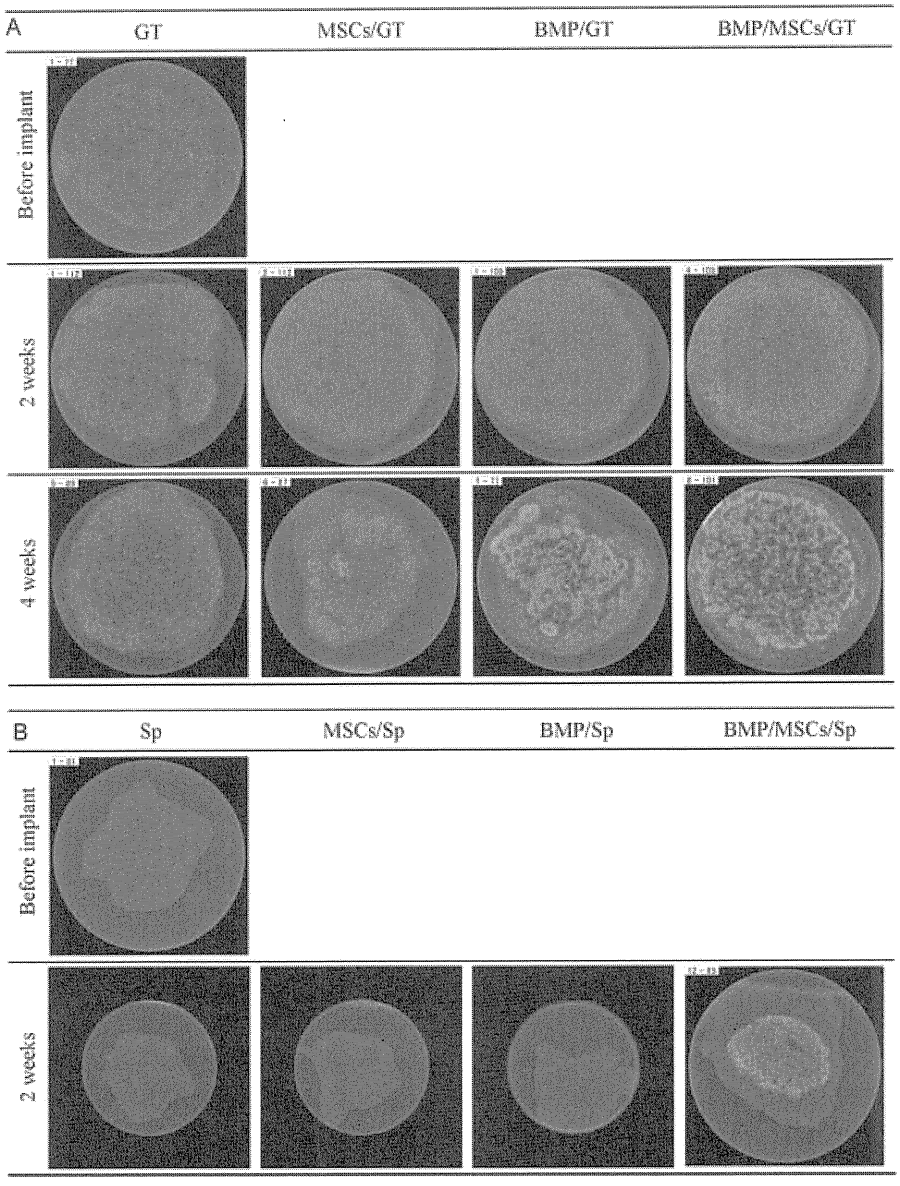

Figure 1. Typical micro-computed tomography (μCT) images of the implants using gelatin-β-TCP (GT) and gelatin (Sp) sponges. Images of various implants using GT (A) and Sp (B) materials after *in vivo* implantation. The MSC–GT, BMP–GT and BMP–MSC–GT implants show high-intensity areas (white) as compared to the image of the GT-alone implant 4 weeks after implantation

which showed abundant bone formation in the BMP–GT and BMP–MSC–GT groups and the *osteocalcin* gene expression profiles.

4. Discussion

Bone marrow-derived MSCs are a well-accepted source of osteogenic cells that can be used in bone tissue engineering. However, it is still a challenge to enhance the proliferation and differentiation of the *in vitro* expanded MSCs for bone tissue engineering, a problem that can be solved by approaches using growth factors (Betz *et al.*, 2008; Chan *et al.*, 2005). A number of factors have been shown to play a role in the osteogenic differentiation of MSCs (Kodama *et al.*, 2009; Maegawa *et al.*, 2007; Raiche and Puleo, 2004; Shimaoka *et al.*, 2004). In this study, we demonstrated that differentiation was greatly enhanced by BMP-2 *in vivo* using gelatin–β-TCP sponge incorporating BMP-2.

GT sponge could be fabricated to function as a release carrier of BMP-2. When BMP-2-incorporated GT sponges were implanted subcutaneously, the BMP-2 was retained in the sponges for at least 1 month and steadily released over that time. *In vivo* bone formation was observed in BMP-2-incorporated GT sponges 4 weeks after implantation in a subcutaneous site in rats (Takahashi *et al.*, 2005a). In this study, we aimed to demonstrate that early bone formation could be achieved by incorporating BMP-2 into GT sponges when combined with MSCs. As expected, we confirmed that new bone was observed in the BMP–MSC–GT and BMP–MSC–Sp groups 2 weeks after implantation. Furthermore, maturation of the new bone tissue was observed in the BMP–MSC–GT after

DOI: 10.1002/term

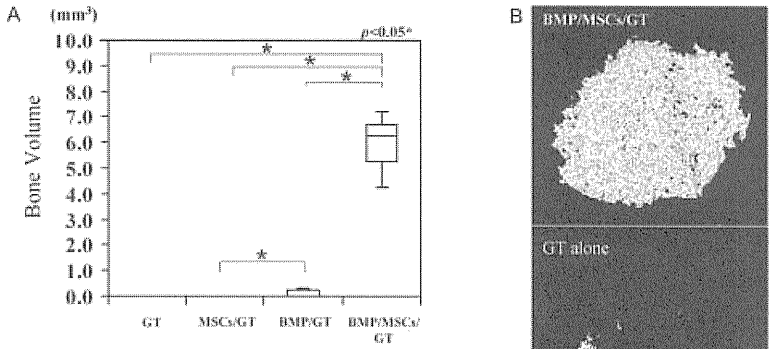

C

Implants	The average bone volume (mm³)	The Number of bone detections
GT alone	0.0043±0.0010	0/5
MSCs/GT composite	0.0057±0.0503	1/5
BMP/GT composites	0.1601±0.1142	4/5
BMP/MSCs/GT composites	5.8698±1.5267	5/5

Figure 2. Bone volume and 3D CT images of implants 4 weeks after subcutaneous implantation ($n = 5$). Bone volume (A) and 3D images (B) were calculated from μCT data. (C) Details of average bone volume and number of bone detections. $^{*}p < 0.05$

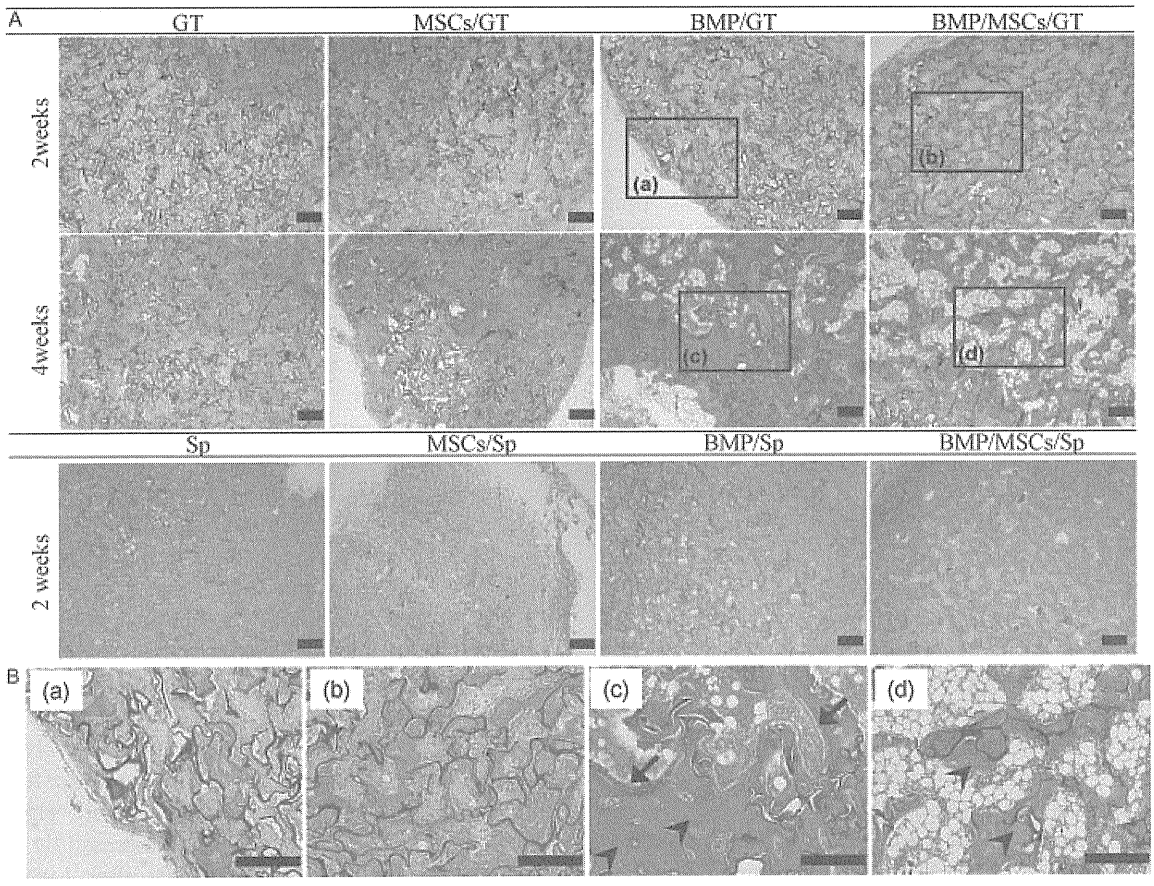

Figure 3. Histological findings of implants using gelatin-β-TCP (GT) and gelatin (Sp) sponges after implantation. (A) In implants using GT, new bone formation is observed in BMP–GT and BMP–MSC–GT implants 2 weeks after implantation. GT-alone and MSC–GT implants exhibit fibrous tissue invasion with no evidence of bone formation. Four weeks after implantation, massive bone formation is observed in the BMP–GT and BMP–MSC–GT implants. The GT-alone and MSC–GT implants exhibited fibrous tissue invasion but the bone formation was hard to detect. In Sp implants, new bone formation was observed in only BMP–MSC–Sp implants. The Sp alone, MSCs/Sp and BMS/Sp implants exhibited fibrous tissue invasion without bone formation. (B) High-magnification images of the rectangular areas of (a–c) and (e) in (A), respectively. Osteoblasts (arrows) and osteocytes (arrowheads) were observed within the newly formed bone. Scale bar = 200 μm

DOI: 10.1002/term

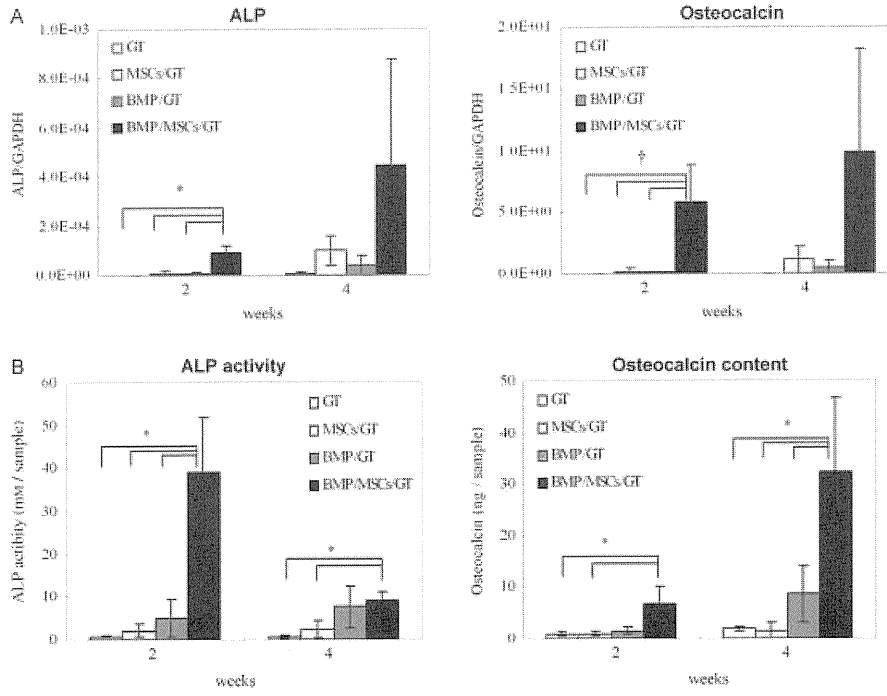

Figure 4. Gene expression and biochemical analysis of alkaline phosphatase (ALP) and osteocalcin in the implants. (A) The gene expression of ALP and osteocalcin were measured by quantitative real-time PCR 2 and 4 weeks after implantation. Values are shown as mean ± SD ($n = 3$). $^{*}p < 0.05$. $^{\dagger}p < 0.01$. (B) ALP activity and osteocalcin content of the implants were measured after 2 and 4 weeks. Implants are GT-alone, MSC–GT, BMP–GT and BMP–MSC–GT. Values are shown as mean ± SD ($n = 4$). $^{*}p < 0.05$

4 weeks. On the other hand, although new bone formation was observed in the BMP–GT group, which was free of MSCs, the volume of new bone was less than in the BMP–MSC–GT and the BMP–MSC–Sp groups. Biochemical analyses of the osteogenic differentiation at the levels of gene (Figure 4A) and protein expressions (Figure 4B) also demonstrated that the highest ALP and osteocalcin was in the BMP–MSC–GT group. These results indicate that the new bone-forming capability of BMP-2 incorporated into GT sponges could be enhanced by supplementation with MSCs.

We previously demonstrated that new bone formation was observed following subcutaneous implantation of MSCs combined with calcium phosphate ceramics, such as HA (Matsushima *et al.*, 2009; Ohgushi and Caplan, 1999; Okamoto *et al.*, 2006). However, the amount of new bone was limited 4 weeks after implantation and could not even be detected after 2 weeks. By adding BMP-2 into the HA ceramics, new bone formation increased, but in the composites of HA and BMP-2 without MSCs it was hard to identify the new bone (Shimaoka *et al.*, 2004). In contrast, the results from the present study clearly demonstrated the bone-forming capability of the BMP–GT implants, indicating the excellent ability of the GT to carry BMP-2. Furthermore, obvious bone formation was detected only 2 weeks after implantation in the BMP–MSC–GT group and extensive bone formation was observed in the composites after 4 weeks. With regard to β-TCP-containing sponge, β-TCP content did not change *in vivo* release behaviour of BMP-2 (Takahashi *et al.*, 2005b). However, in comparison with gelatin sponge incorporating other ceramics granules, such as HA, αTCP and alumina, gelatin-β-TCP sponges exhibited the highest ALP activity of MSCs among them (Takahashi *et al.* 2005b). These findings demonstrate the superior properties of GT sponge compared to HA ceramics.

One other disadvantage of the calcium phosphate ceramics is that absorption of the ceramics takes several months to years, and in the case of HA ceramics they are considered to be essentially non-absorbable. It is well known that the bone formation process followed by the absorptive capability of the implant, more specifically bone substitution, is an important factor for bone graft implantation in clinical situations. In this regard HA ceramics are not ideal materials, due to their poor absorption (Barrere *et al.*, 2006). However, too-early absorption hampers bone formation, as was seen in the BMP–MSC–Sp group as a result of the rapid absorptive properties of gelatin. Only one sample of the BMP–MSC–Sp group showed bone formation after 2 weeks, but none of the implants or bone tissue was detected after 4 weeks. We improved the absorption properties of the gelatin, which is known to have relatively rapid absorption properties compared with HA. Using the gelatin β-TCP sponge (GT), we successfully showed early bone formation with osteoblasts after 2 weeks and extensive bone tissue with many osteocytes in abundant bone matrix after 4 weeks.

5. Conclusion

Overall, the results presented here demonstrate the usefulness of the GT, BMP-2 and MSC composites as an

DOI: 10.1002/term

innovative osteoinductive bone graft substitute. Currently, gelatin, β-TCP, BMP-2 and MSCs have been used for various purposes in regenerative medicine. The ability of BMP-2 incorporated into GT sponges to form new bone could be enhanced by supplementation with MSCs. Moreover, the combination of GT sponge, BMP-2 and MSCs led to early bone formation. Due to the extensive *in vivo* bone formation together with reasonable GT absorption, the composites could be applied in tissue engineering aimed at bone tissue reconstruction.

Acknowledgements

This work was supported in part by the Project for Realization of Regenerative Medicine from the Ministry of Education, Culture, Sports, Science and Technology, Japan.

References

Barrere F, van Blitterswijk CA, de Groot K. 2006; Bone regeneration: molecular and cellular interactions with calcium phosphate ceramics. *Int J Nanomed* **1:** 317–332.

Betz VM, Betz OB, Harris MB, *et al.* 2008; Bone tissue engineering and repair by gene therapy. *Front Biosci* **13:** 833–841.

Chan J, O'Donoghue K, De la Fuente J, *et al.* 2005; Human fetal mesenchymal stem cells as vehicles for gene delivery. *Stem Cells* **23:** 93–102.

Giannoudis PV, Dinopoulos H, Tsiridis E. 2005; Bone substitutes: an update. *Injury* **36:** 20–27.

Ikeuchi M, Dohi Y, Horiuchi K, *et al.* 2002; Recombinant human bone morphogenetic protein-2 promotes osteogenesis within atelopeptide type I collagen solution by combination with rat cultured marrow cells. *J Biomed Mater Res* **60:** 61–69.

Kawate K, Yajima H, Ohgushi H, *et al.* 2006; Tissue-engineered approach for the treatment of steroid-induced osteonecrosis of the femoral head: transplantation of autologous mesenchymal stem cells cultured with β-tricalcium phosphate ceramics and free vascularized fibula. *Artif Organs* **30:** 960–962.

Kodama N, Nagata M, Tabata Y, *et al.* 2009; A local bone anabolic effect of rhFGF2-impregnated gelatin hydrogel by promoting cell proliferation and coordinating osteoblastic differentiation. *Bone* **44:** 699–707.

LeGeros RZ. 2008; Calcium phosphate-based osteoinductive materials. *Chem Rev* **108:** 4742–4753.

Maegawa N, Kawamura K, Hirose M, *et al.* 2007; Enhancement of osteoblastic differentiation of mesenchymal stromal cells cultured by selective combination of bone morphogenetic protein-2 (BMP-2) and fibroblast growth factor-2 (FGF-2). *J Tissue Eng Regen Med* **1:** 306–313.

Maniatopoulos C, Sodek J, Melcher AH. 1988; Bone formation *in vitro* by stromal cells obtained from bone marrow of young adult rats. *Cell Tissue Res* **254:** 317–330.

Matsushima A, Kotobuki N, Tadokoro M, *et al.* 2009; *In vivo* osteogenic capability of human mesenchymal cells cultured on hydroxyapatite and on β-tricalcium phosphate. *Artif Organs* **33:** 474–481.

Morishita T, Honoki K, Ohgushi H, *et al.* 2006; Tissue engineering approach to the treatment of bone tumors: three cases of cultured bone grafts derived from patients' mesenchymal stem cells. *Artif Organs* **30:** 115–118.

Nishikawa M, Myoui A, Ohgushi H, *et al.* 2004; Bone tissue engineering using novel interconnected porous hydroxyapatite ceramics combined with marrow mesenchymal cells: quantitative and three-dimensional image analysis. *Cell Transplant* **13:** 367–376.

Ohgushi H, Caplan AI. 1999; Stem cell technology and bioceramics: from cell to gene engineering. *J Biomed Mater Res* **48:** 913–927.

Ohgushi H, Dohi Y, Katuda T, *et al.* 1996; *In vitro* bone formation by rat marrow cell culture. *J Biomed Mater Res* **32:** 333–340.

Ohgushi H, Kitamura S, Kotobuki N, *et al.* 2004; Clinical application of marrow mesenchymal stem cells for hard tissue repair. *Yonsei Med J* **45:** 61–67.

Ohgushi H, Kotobuki N, Funaoka H, *et al.* 2005; Tissue engineered ceramic artificial joint – *ex vivo* osteogenic differentiation of patient mesenchymal cells on total ankle joints for treatment of osteoarthritis. *Biomaterials* **26:** 4654–4661.

Okamoto M, Dohi Y, Ohgushi H, *et al.* 2006; Influence of the porosity of hydroxyapatite ceramics on *in vitro* and *in vivo* bone formation by cultured rat bone marrow stromal cells. *J Mater Sci Mater Med* **17:** 327–336.

Raiche AT, Puleo DA. 2004; Cell responses to BMP-2 and IGF-I released with different time-dependent profiles. *J Biomed Mater Res A* **69A:** 342–350.

Reddi AH, Cunningham NS. 1993; Initiation and promotion of bone differentiation by bone morphogenetic proteins. *J Bone Miner Res* **8:** S499–502.

Ruhe PQ, Boerman OC, Russel FGM, *et al.* 2006; *In vivo* release of rhBMP-2 loaded porous calcium phosphate cement pretreated with albumin. *J Mater Sci Mater Med* **17:** 919–927.

Shimaoka H, Dohi Y, Ohgushi H, *et al.* 2004; Recombinant growth/differentiation factor-5 (GDF-5) stimulates osteogenic differentiation of marrow mesenchymal stem cells in porous hydroxyapatite ceramic. *J Biomed Mater Res A* **68A:** 168–176.

Tabata Y. 2008; Current status of regenerative medical therapy based on drug delivery technology. *Reprod Biomed Online* **16:** 70–80.

Tabata Y. 2009; Biomaterial technology for tissue engineering applications. *J Roy Soc Interface* **6:** S311–324.

Tabata Y, Nagano A, Ikada Y. 1999; Biodegradation of hydrogel carrier incorporating fibroblast growth factor. *Tissue Eng* **5:** 127–138.

Takahashi Y, Yamamoto M, Tabata Y. 2005a; Enhanced osteoinduction by controlled release of bone morphogenetic protein-2 from biodegradable sponge composed of gelatin and β-tricalcium phosphate. *Biomaterials* **26:** 4856–4865.

Takahashi Y, Yamamoto M, Tabata Y. 2005b; Osteogenic differentiation of mesenchymal stem cells in biodegradable sponges composed of gelatin and β-tricalcium phosphate. *Biomaterials* **26:** 3587–3596.

Yoshikawa H, Myoui A. 2005; Bone tissue engineering with porous hydroxyapatite ceramics. *J Artif Organs* **8:** 131–136.

Zegzula HD, Buck DC, Brekke J, *et al.* 1997; Bone formation with use of rhBMP-2 (recombinant human bone morphogenetic protein-2). *J Bone Joint Surg Am* **79A:** 1778–1790.

Int. J. Mol. Sci. **2012**, *13*, 5528-5541; doi:10.3390/ijms13055528

OPEN ACCESS
International Journal of
Molecular Sciences
ISSN 1422-0067
www.mdpi.com/journal/ijms

Article

Early Fixation of Cobalt-Chromium Based Alloy Surgical Implants to Bone Using a Tissue-engineering Approach

Munehiro Ogawa [1], Yasuaki Tohma [1,2,3], Hajime Ohgushi [3,*], Yoshinori Takakura [1] and Yasuhito Tanaka [1]

[1] Department of Orthopedic Surgery, Nara Medical University, 840 Shijyo-cho, Kashihara, Nara 634-8522, Japan; E-Mails: mogawa@naramed-u.ac.jp (M.O.); tohma@wnara.hosp.go.jp (Yasua.T.); ashitakakura@leto.eonet.ne.jp (Yo.T.); yatanaka@naramed-u.ac.jp (Yasuh.T.)

[2] Department of Orthopedic Surgery, National Hospital Organization Nara Medical Center, Nara 630-8053, Japan

[3] Health Research Institute, National Institute of Advanced Industrial Science and Technology (AIST), Amagasaki, Hyogo 661-0974, Japan

* Author to whom correspondence should be addressed; E-Mail: hajime-ohgushi@aist.go.jp; Tel.: +81-6-6494-7807; Fax: +81-6-6491-5028.

Received: 24 March 2012; in revised form: 25 April 2012 / Accepted: 3 May 2012 / Published: 9 May 2012

Abstract: To establish the methods of demonstrating early fixation of metal implants to bone, one side of a Cobalt-Chromium (CoCr) based alloy implant surface was seeded with rabbit marrow mesenchymal cells and the other side was left unseeded. The mesenchymal cells were further cultured in the presence of ascorbic acid, β-glycerophosphate and dexamethasone, resulting in the appearance of osteoblasts and bone matrix on the implant surface. Thus, we succeeded in generating tissue-engineered bone on one side of the CoCr implant. The CoCr implants were then implanted in rabbit bone defects. Three weeks after the implantation, evaluations of mechanical test, undecalcified histological section and electron microscope analysis were performed. Histological and electron microscope images of the tissue engineered surface exhibited abundant new bone formation. However, newly formed bone tissue was difficult to detect on the side without cell seeding. In the mechanical test, the mean values of pull-out forces were 77.15 N and 44.94 N for the tissue-engineered and non-cell-seeded surfaces, respectively. These findings indicate early bone fixation of the tissue-engineered CoCr surface just three weeks after implantation.

Keywords: implant-bone interface; cobalt chromium alloy; marrow mesenchymal cell; osteogenesis; tissue engineering

1. Introduction

Initial implant fixation is critical for long term performance of prosthetic arthroplasty. Therefore, implants ability to provide early, stable, and osseous fixation is required to ensure success in clinical cases. Incomplete anchorage between the implants surface and bone might lead to aseptic loosening and subsequent failure in the prostheses [1]. Cobalt chromium (CoCr) based alloys have been widely used for prosthetic arthroplasty. Their mechanical properties seem to be suitable material for the purpose of total hip and knee joint arthroplasty [2,3]. Recent reports, however, have raised some questions concerning the osteogenic function of the CoCr alloy, which might cause loosening of arthroplasty using this alloy [4,5].

We have developed a novel method to solve the problem of loosening of alumina ceramics ankle arthroplasty using a tissue engineering approach [6]. Mesenchymal cells residing in bone marrow can differentiate into osteoblasts and undergo mineralization when they are cultured in the presence of ascorbic acid, β-glycerophosphate and dexamethasone [7–10]. On the basis of these findings, we have succeeded in fabricating a tissue engineered alumina ceramics implant with excellent osteogenic function, which improves bone-implant fixation. Specifically, the method involves culturing the mesenchymal cells on the alumina ceramics implant surface prior to implantation. The culture shows osteogenic differentiation of the cells; *i.e.*, appearance of osteoblasts which fabricate bone matrix on the alumina ceramics implant. Previously, we reported that tissue engineered alumina ceramics caused early bone ingrowth in the rabbit model. In brief, the osteoblast/bone matrix formed on alumina ceramics can show further *in vivo* osteogenic function resulting in a stable interface between the tissue engineered alumina ceramics surface and the host bone [11]. Moreover, we also reported successful clinical cases of the tissue engineered alumina ceramics ankle arthroplasty using mesenchymal cells derived from patient bone marrow. These cases showed stable interface between the tissue engineered ceramics surface and host bone even some years post operation [6].

In the present study, we focused on CoCr alloys and hypothesized that this tissue engineering approach could be suitable for not only alumina ceramics implant but also CoCr based alloy implant in order to solve the inherent problems of this alloy such as loosening. For this purpose, we conducted the following study in which CoCr alloy implants were loaded with cultured mesenchymal cells and implanted in rabbit bone. Three weeks after the implantation, mechanical as well as histological analyses were performed to demonstrate early fixation of the alloy to the bone.

2. Results and Discussion

2.1. In Vitro *Experiment*

We performed a tissue engineering approach for CoCr based alloy implant in order to solve problems of this alloy concerning the osteogenic property. The approach utilized marrow cells, which contain

mesenchymal cells having osteogenic functions, and consisted of three steps: (1) Proliferation of mesenchymal cells from rabbit bone marrow by culture, (2) Osteogenic differentiation of the culture expanded cells resulting in the appearance of bone-forming osteoblasts together with bone matrix formation on the CoCr alloy and (3) Implantation of the the CoCr alloy in the same rabbit. To obtain the mesenchymal cells for step 1, we aspirated about 2 mL of rabbit bone marrow by needle. Therefore, the marrow harvest was performed in a minimally-invasive manner and the 2 mL marrow was enough to expand the number of mesenchymal cells for the experiments. During step 2, the culture mesenchymal cells differentiated into bone forming osteoblasts. The osteoblasts synthesize extracellular matrix in which bone mineral exist. The mineral can be stained with alizarin red S (Figure 1), and we conducted the stain to confirm bone matrix formation [9]. As seen in Figure 1, Alizarin red S was positive on the cell loaded surface. However, staining was negative on the non-cell loaded surface. The results confirmed that the surface of CoCr alloy was covered with osteoblasts and bone matrix and demonstrated the fabrication of tissue engineered CoCr alloy implants.

Figure 1. Alizarin red S stain of CoCr based alloy. Alizarin red S stain of the mesenchymal cells loaded (right) and non-cell loaded (left) surface of the alloy after *in vitro* osteogenic culture. Red color indicating bone mineral is only seen in the right figure.

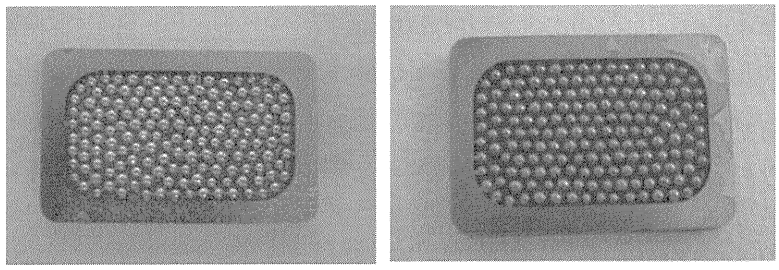

2.2. Mechanical Testing

After the *in vitro* culture of mesenchymal cells on the CoCr alloy, we performed step 3. This consisted of *in vivo* implantation, to examine whether the tissue engineered CoCr implants exhibited the osteogenic function resulting in tight fixation of the implants to host bone. After creation of a bone defect in the rabbit tibia, we inserted the CoCr implants as described later in the methods section. The implantation was performed on the same rabbit from which we harvested the bone marrow. The pull-out test was performed on 6 tibias after 3 weeks implantation. In all cases, the implants detached from the non-cell loaded side. Then, the implant was again placed in the grip of the testing machine to evaluate pull-out force between the cell loaded implant surface and the bone on the opposite side. The mean values of pull-out force are shown in Figure 2. The pull-out force of the cell loaded side was greater than that of the non-cell loaded side. The mean values of pull-out forces were 77.15 N and 44.94 N for the cell loaded side and non-cell loaded side, respectively. The differences of the mean values of pull-out force between non-cell loaded side and cell loaded side were significant ($p = 0.046$) (Figure 2). After the pull-out test of non-cell loaded side, the bare surface of the CoCr implants was seen. Remnants of bone tissue were found after the detachment of cell loaded side.

Figure 2. Pull-out forces of the implants after 3 weeks implantation (n = 6). The data are indicated by box plot. This plot is used to visually summarize and compare groups of data. The box plot uses the median, the approximate quartiles, and the lowest and highest data points to convey the level, spread, and symmetry of a distribution of data values. The parameters used in this figure are as follows: 50 percentiles as median, median is shown as a horizontal bar in the box.; 25 and 75 percentiles as a concentration indicator, 75 percentiles is shown as a top of the box and 25 percentiles is shown as a bottom of it; minimum and maximum data as a distribution range.

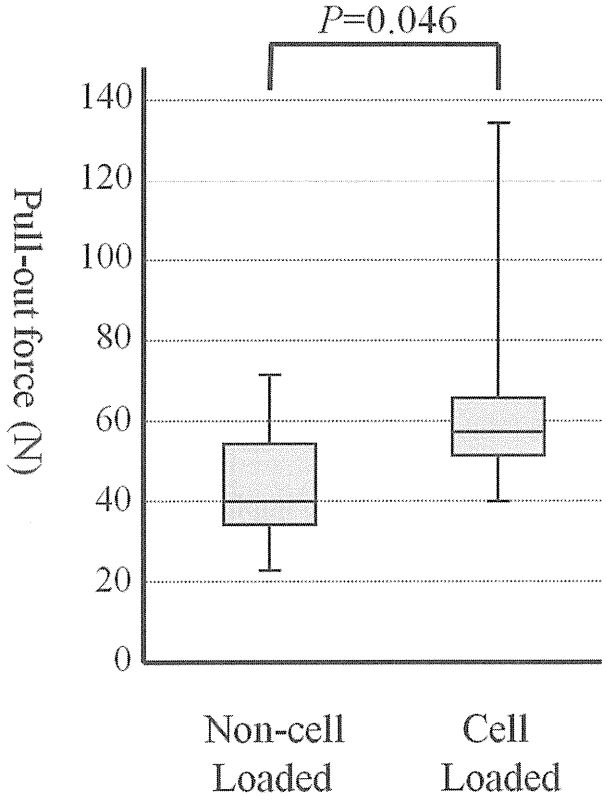

2.3. Histological Examination and Electron Microscope Analysis

Histological examination of the implants of the non-cell loaded surface showed a connective tissue layer at the interface between bone and the implant surface. However, there was no bone ingrowth into the spaces between the CoCr based alloy beads on the implant surface. On the other hand, the cell loaded surface showed new bone ingrowth into the spaces between the CoCr based alloy beads on the implant surface. Thus, extensive newly formed bone was detected in the tissue engineered implant surface and these histological findings verify the results of mechanical testing which demonstrate the tight fixation of the cell loaded implant surface and host bone (Figure 3).

Electron microscope analysis was consistent with the results of histological examination. Electron microscope images of the cell loaded surface exhibited abundant new bone formation. However, newly formed bone tissue was difficult to detect on the side of the non-cell loaded surface (Figure 4).

Figure 3. Toluidine blue-stained sections of the implants after 3 weeks. The cell loaded surface (upper images) shows extensive new bone formation into the spaces among the CoCr beads on the implant surface. The non-cell loaded surface (lower images) shows only connective tissue layers. Right figures are magnified images of the rectangular areas in the left figures.

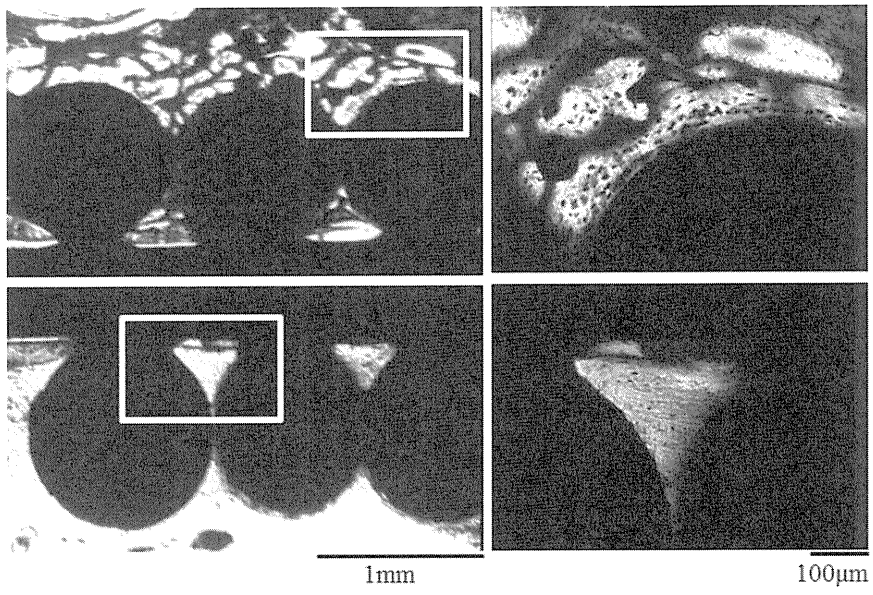

Figure 4. Electron microscope images of the implants after 3 weeks. As seen in Figure 6, abundant new bone formation is seen on the cell loaded surface (upper figures) but not on non-cell loaded surface (lower figures). Right figures are magnified images of the rectangular areas in the left figures.

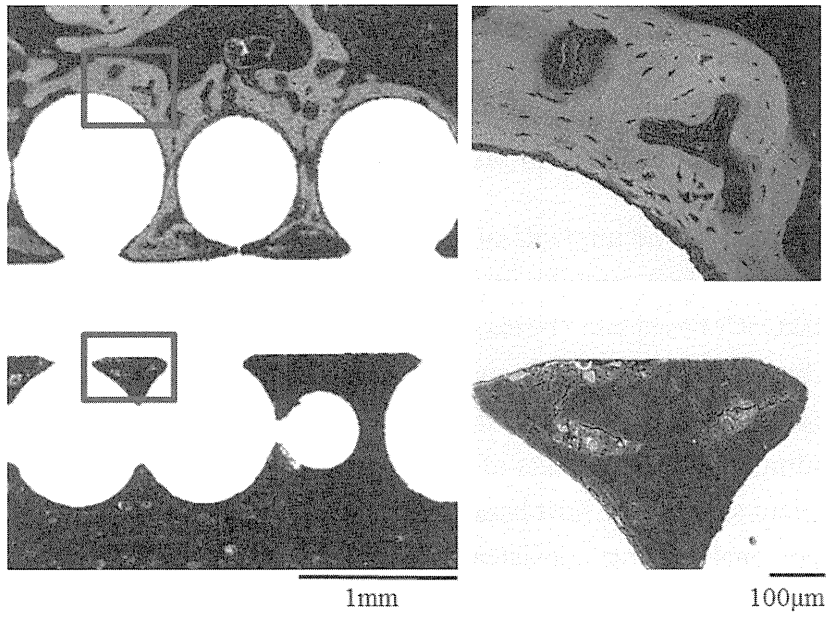

2.4. Discussion

Metallic biomaterials have a wide range of applications as prosthetic materials for joint arthroplasty in the orthopedic field. In recent years, the use of Titanium (Ti) based alloys as biomaterials have increased